CHAPTER 4

THE GROWTH OF SILICON RIBBONS FOR PHOTOVOLTAICS BY EDGE-SUPPORTED PULLING (ESP)

T.F. CISZEK

Solar Energy Research Institute
Golden, CO 80401, USA

Silicon Processing for Photovoltaics I, edited by C.P. Khattak and K.V. Ravi

Contents

1. Introduction

Two ribbon growth methods for silicon date back to the mid 1960s. These are dendritic web growth (Dermatis and Faust, 1963), and Stepanov growth (Boatman and Goundry, 1967). Edge-defined film-fed growth (EFG) applied first to sapphire (LaBelle et al., 1971), and later to silicon (Ciszek, 1972), was the first method directed to terrestrial photovoltaic (PV) applications. In the mid-1970s, many new growth methods specifically intended for low-cost PV use appeared. Table 1 lists these methods along with earlier and later techniques. Edge-supported pulling (ESP) is a relatively new technique (Ciszek and Hurd, 1980). Other recently introduced methods include melt spinning of various types (Tsuya et al., 1980; Maeda and Yokoyama, 1982), and interface-controlled crystallization (Dietl et al., 1981). A comprehensive review of the various sheet growth methods has been made (Ciszek, 1984).

In edge-supported pulling, an elongated liquid silicon meniscus is formed between two thin parallel filaments that move through the liquid. The ends of the meniscus are pinned at the filaments. The base rises from the free liquid surface of the molten silicon. The meniscus top is originally attached to a silicon seed or other cross member, where sheet growth is initiated. As the filaments move through the liquid, the attached cross

Table 1
Si sheet growth methods arranged chronologically.

Dendritic web (WEB, 1963)	Capillary action shaping technique (CAST, 1977)
Stepanov (S, 1967)	Contiguous capillary coating (CCC, 1977/ S-WEB, 1982)
Edge-defined, film-fed growth (EFG, 1972)	Inverted Stepanov (IS, 1977)
Horizontal ribbon growth (HRG, 1975/ LASS, 1980)	Roller quenching (RQ, 1979)
Ribbon-against-drop (RAD, 1976)	Edge-supported pulling (ESP, 1980)
Ribbon-to-ribbon zoning (RTR, 1976)	Interface-controlled crystallization (ICC, 1981)
Silicon-on-ceramic (SOC, 1976)	

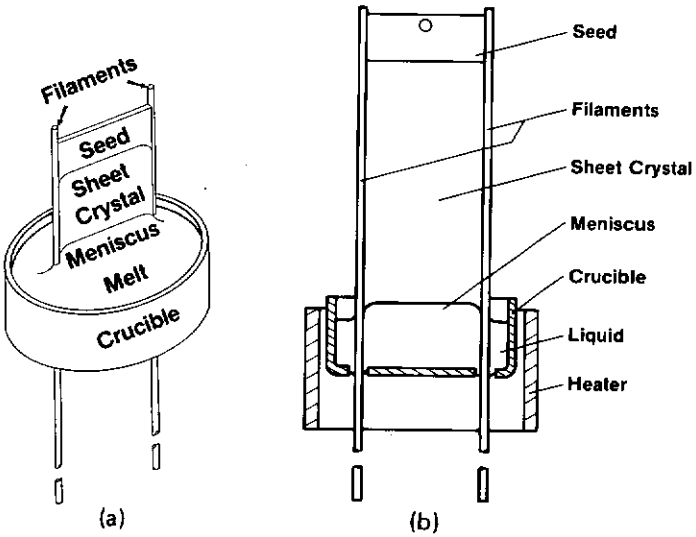

Fig. 1. The edge-supported pulling (ESP) process shown schematically in (a) isometric and (b) longitudinal section views.

member moves away from the liquid surface, and a sheet continually solidifies between the filaments. The top of the meniscus is attached to the solid/liquid interface of the sheet. A vertical pulling mode of the ESP ribbon growth process is shown schematically in fig. 1.

The high meniscus and the meniscus edge pinning that are characteristic of ESP growth allow easy control of the growth process and minimize its susceptibility to mechanical and thermal perturbations. The high meniscus further contributes to enhanced crystal grain size. ESP is similar to dendritic web growth (Dermatis and Faust, 1963), but since filaments are used instead of silicon dendrites to stabilize the meniscus edges, the need for controlled supercooling to propagate dendrites is not present. Thus, thermal control requirements are much less (±5–10°C). On the other hand, since the filaments are foreign substances, they lead to grain nucleation. However, because the filaments are in contact with the silicon only at the edges, their effect on crystal perfection is not as detrimental as that seen with sheet growth on large-area foreign substrates (Belouet et al., 1978; Zook et al., 1980).

Each of the 15 Si sheet growth methods listed in table 1 can be assigned one of the three general meniscus shapes depicted in fig. 2. The height of

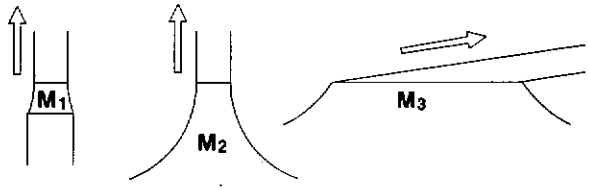

Fig. 2. Three generalized meniscus configurations encountered in silicon sheet growth.

the M_1 meniscus is of the order of the sheet thickness t. The M_2 meniscus rises from a broad base (at the crucible melt level, for example) to the sheet interface and typically has a height on the order of 6–7 mm. The M_3 meniscus is characterized by a large solid/liquid interface area compared to wt, where w is the ribbon width.

The five ribbon processes having the M_1 meniscus are S, EFG, RTR, CAST, and IS. In these processes, there is close physical proximity between the melt shaping device (or feedstock ribbon in the case of RTR) and the solid/liquid interface of the growing ribbon. Implications of this are potential thermal and mechanical control difficulties. Furthermore, if the shaper is a foreign material (all cases except RTR), the close proximity can lead to significant incorporation of impurities in the Si sheet.

Vertical ESP is one of the methods having an M_2 meniscus. Others are WEB, RAD, SOC, CCC, and S-WEB. A general implication of the high M_2 meniscus is a greater tolerance of mechanical and thermal perturbations, since no melt shaper is close to the solid/liquid interface.

The ribbon processes that use an extended, large-area M_3 meniscus are HRG, LASS, the SCIM version of SOC, RQ, and ICC. These techniques achieve a very fast growth rate through (a) use of a solid/liquid interface area which is greater than wt, the cross-sectional area of the ribbon, and (b) efficient extraction of the latent heat of fusion. Since the heat of fusion is liberated over an area larger than wt, the amount to be dissipated per unit area is less than for M_1 or M_2 menisci. Also, because the ribbon is wedge shaped at the growth front, the heat loss surface from which the latent heat is to be removed is very close and nearly parallel to the surface where heat is generated (the separation distance is less than or equal to t). Both of these factors contribute to efficient heat removal and high growth rates. Horizontal or low-angle ESP growth of silicon sheets (Ciszek and Hurd, 1981) has these same advantages and in addition provides easy edge definition and thermal control.

2. Meniscus characteristics

The height of the meniscus from which the ESP silicon sheet solidifies and the meniscus height on the filaments will be discussed with reference to fig. 3. If a thin solid plate is immersed vertically in a liquid that perfectly wets it, a meniscus will rise on the plate to a height a. The value of a can be deduced from Laplace's equation for the pressure change across a gas/liquid interface, and is given by

$$a = (2\sigma/\varrho g)^{1/2}, \tag{1}$$

where σ is the solid/liquid surface tension (720 dyn/cm for Si), ϱ is the liquid density (2.53 g/cm^3 for Si), and g is the gravitational acceleration. If the liquid does not perfectly wet the plate, there is a non-zero contact angle θ (approximately 11° for silicon liquid against silicon solid) and the expression for meniscus height h is

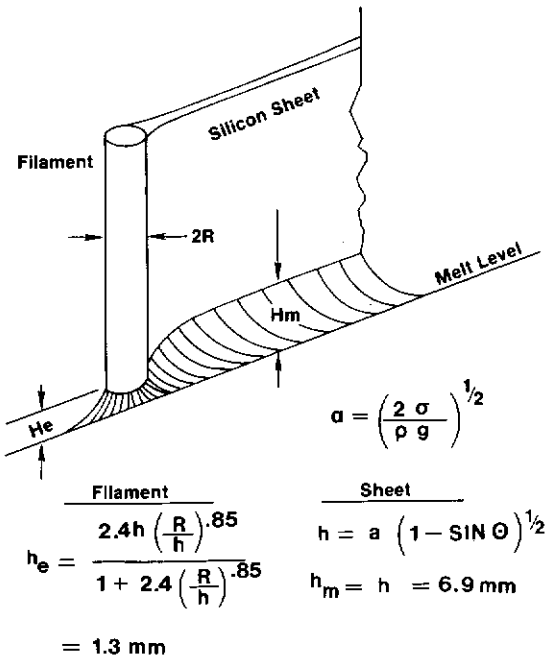

Fig. 3. Meniscus heights at the edge h_e and mid-region h_m for silicon ESP growth with 1 mm diameter graphite filaments.

$$h = a(1 - \sin\Theta)^{1/2}. \tag{2}$$

The meniscus height in the mid-region of an ESP sheet's solid/liquid interface is reasonably well represented by eq. (2), which gives a numerical value of 6.9 mm for h_m (meniscus height in the mid-region).

The meniscus height of the liquid silicon in contact with the filaments at the edge of the sheet is more complex to analyze even for the special case of filaments with a circular cross section. White and Tallmadge (1965) have analyzed the case of isolated vertical wires of radius R in a perfectly wetting liquid using numerical integration methods. A semiempirical expression for meniscus height h_f on the filament of the form

$$h_f = \frac{2.4a(R/a)^{0.85}}{1 + 2.4(R/a)^{0.85}} \tag{3}$$

was found to agree with the numerical integration results to within 1% for $0.006 < R/a < 3.0$. If we assume that h from eq. (2) can be substituted for a in eq. (3) when the liquid does not perfectly wet the filament, then the expression for meniscus height on the filament at the sheet edge, h_e, is given by

$$h_e = \frac{2.4h(R/h)^{0.85}}{1 + 2.4(R/h)^{0.85}}. \tag{4}$$

Since h is a function of contact angle θ, h_e will be different for different filament materials. Useful filament materials for silicon growth include carbon, silicon carbide, silicon dioxide, silicon nitride, and mullite. The contact angles range from about 20° to nearly 90°. Hence, h_e can vary from about 0 to 1.4 mm. It is interesting to note that even though silicon dioxide and mullite are not well wetted by silicon, filaments and even bridge members of these materials will function for ESP growth. The use of various filament materials will be discussed in section 4.

A consequence of $h_m > h_e$ is that the solid/liquid interface is concave toward the liquid, in the plane of the sheet. Hence, spurious grains nucleated at the filaments tend to propagate toward the mid-region of the sheet.

3. Silicon sheet growth procedures

The apparatus for ESP growth consists of a vertical quartz tube furnace with water-cooled end plates containing an argon ambient. A translatable,

rotatable shaft passes through the bottom plate. A graphite crucible holder and a concentric opaque insulator tube are mounted on this shaft. The crucible holder contains a clear fused quartz crucible, which in turn holds the liquid silicon. Heat is provided by an external induction coil operating at 350–500 kHz. A long vertical oval tube is mounted on the top plate of the furnace and serves as both the exit port for the argon purge gas and the pulling port through which the silicon sheet passes.

Argon is purged through the furnace from the bottom to the top. In addition, an argon jet is directed at each edge of the growing silicon sheet. By varying the gas flow at the edges, lateral temperature uniformity can be adjusted. A third argon jet is used to keep SiO deposits from forming on the quartz furnace tube in the viewing area.

For vertical ESP growth of long sheets, the filaments are introduced through the bottom of the melt via two holes approximately 2 mm in diameter in the quartz crucible bottom. The holes serve as guides for the filaments, and their spacing determines the ribbon width. Two larger holes (approximately 8 mm in diameter) are present in the graphite susceptor, concentric with the holes in the crucible. These holes do not contact the filaments, whereas the crucible holes do. This is acceptable for carbon-based filaments. In the case of filament materials that stick to the quartz crucible at high temperatures (e.g., quartz filaments) a more sophisticated filament guidance mechanism is necessary. Here, the filaments must be kept from contacting the edges of the holes in the crucible bottom. One way of doing this is to place filament guides below the large holes in the susceptor bottom. The guides must be precisely aligned with the crucible holes. Alternatively, a different crucible material can be used. For example, the growth of ESP sheets from carbon crucibles with quartz filaments has been reported by Cook and Sachs (1982).

A study that determined the permissible operating range for melt heights and entrance hole diameters in quartz crucibles was conducted by Hurd and Ciszek (1982). To test the limits of leaking, silicon was added to a crucible with two holes equal in diameter in an evacuated furnace (10^{-4} Torr). Four different hole diameters were investigated using four separate crucibles. To prevent large area wetting of the exterior crucible bottom by liquid silicon, the quartz near the holes was shaped to bulge down slightly. This shape creates a barrier to the spreading of drops, preventing their contact line to the crucible from moving out beyond the hole rim onto the crucible bottom. Due to the approximate 90° silicon-quartz contact angle, for the drop contact to increase in diameter, the surface area of the drop

would have to increase beyond the value that satisfies the condition of minimum surface energy for the meniscus. Instead of spreading over the crucible bottom, the silicon forms a contained drop that contacts only the hole rim. All sheets were grown with this hole rim shape.

The silicon melt level was slowly raised until at a certain melt height, dependent on the hole diameter, silicon would begin to leak from the holes. Silicon freely flowed out of the holes until stable menisci were present in both holes. When leaking stopped, the RF heating was turned off, allowing the silicon to cool. For each crucible, the quantity of silicon spilling out of the bottom of the crucible was subtracted from the original quantity of silicon added. From this weight, we calculated a melt height for each hole diameter. The final stable melt height h_s at which leaking stopped both for silicon in a quartz crucible in vacuum and for water in a polypropylene beaker in room air is shown in fig. 4 as a function of inverse hole diameter, $1/\phi$. The reported hole diameters are the average diameters

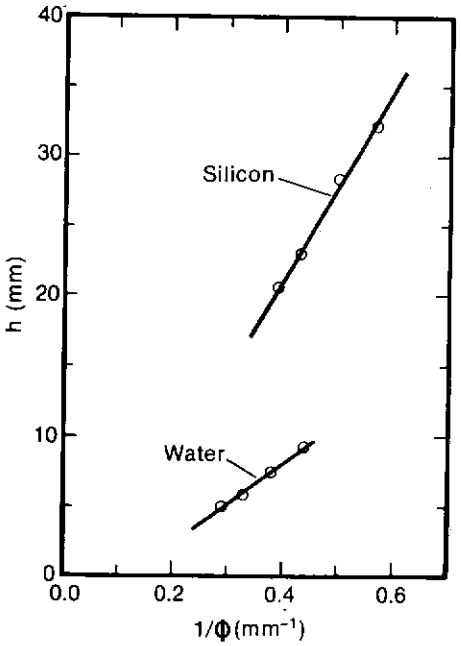

Fig. 4. Stable liquid height h_s as a function of inverse hole diameter ($1/\varphi$) for silicon–quartz–vacuum and water–polypropylene–air.

perpendicular to the hole axis, measured before the experiment. Due to the rounded edges of the hole rims, the actual rim wetting diameters were slightly larger than the reported hole diameters. The actual values could not always be measured after the silicon solidified due to cracking of the silicon and quartz after solidification.

The silicon data were fit through a least squares approximation for the four diameters. The following relationship was found to agree with all four melt heights within 1.8%:

$$h_s = 67.4/\phi - 5.82. \tag{5}$$

Both h_s and ϕ are in millimeters.

Growth of silicon sheets was repeatedly conducted with approximately 2 mm diameter holes and a melt height of about 13 mm using rigid graphite filaments in an argon atmosphere. The melt did not leak from the crucibles even though the drop meniscus was perturbed by the repeated introduction of rigid filaments through the drop. The melt height used was about one-half the maximum stable melt height from fig. 4. By extending the results of perturbing a stable meniscus of water in polypropylene, we project that silicon will not leak when the stable hole meniscus is perturbed by a wettable or nonwettable filament if the liquid level in the crucible is below the stable melt height. Observations after freezing indicate that the silicon meniscus was confined to the hole rim for all diameters tested at all melt heights within the stable region. The filament did not have to be coaxial with the hole for the melt to be retained.

Sheet growth is initiated by heating the silicon in the crucible sufficiently to obtain good wetting at the liquid meniscus attachment to the seed or cross-member. The temperature is then reduced to instigate freezing of the upper meniscus on the cross-member, and the filament assembly is pulled upward so that continued freezing of the top of the meniscus forms a sheet of silicon between the filaments.

Because of the large meniscus height and the pinning of the meniscus at the edges, this growth process is relatively insensitive to mechanical and thermal perturbations, and little thermal control is necessary (±10°C). As seen in fig. 5, growth can be conducted with a large ratio of sheet width to crucible size and without elaborate heat shields and afterheaters characteristic of many ribbon growth techniques. Sheet thickness is, of course, affected by thermal changes even though they may not be severe enough to catastrophically disrupt growth. We have grown 5 cm wide sheets from 5.5 cm I.D. crucibles using the hot zone shown in fig. 5. The details of seed attachment are shown in fig. 6.

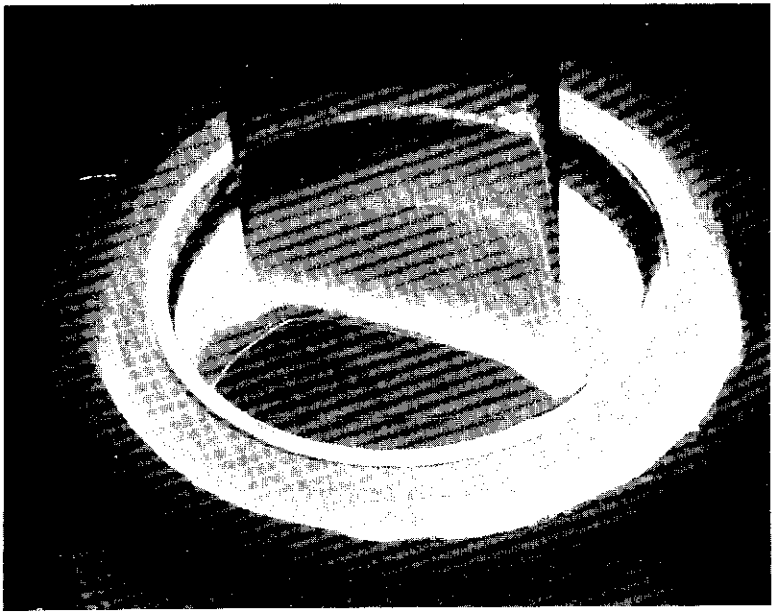

Fig. 5. Hot-zone region for growth of ESP ribbons.

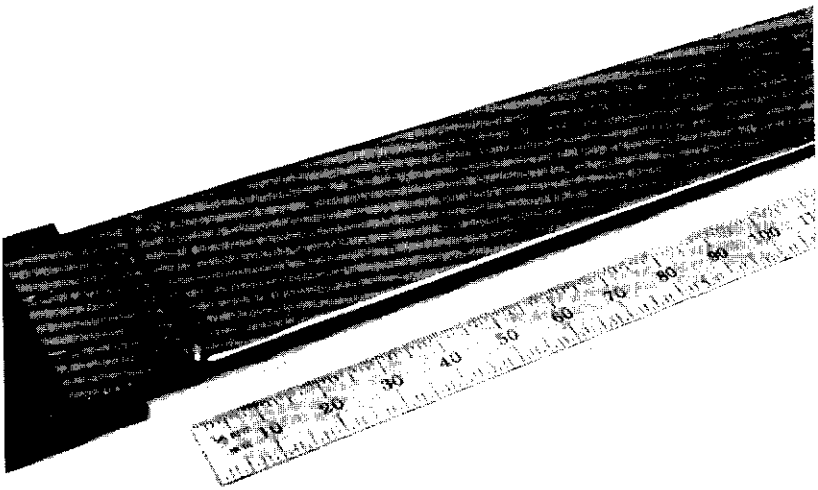

Fig. 6. Silicon sheet grown by edge-supported pulling using rigid graphite filaments.

Sheet thickness is also affected by pulling speed. Faster speeds and/or higher temperatures produce thinner ribbons. We have achieved sustained speeds of up to 3 cm/min with graphite filaments and 4 cm/min with quartz filaments. Momentary speeds up to 9 cm/min were also achieved with quartz filaments.

Thermal stresses and buckling of the sheet have been observed at 100 mm widths (Cooks and Sachs, 1982) indicating that more attention must be paid to thermal profiles during cooling of wide sheets. This somewhat reduces the simplicity of the growth process.

4. Filament materials

Ten different filament materials were experimentally investigated by Ciszek et al. (1982) for such parameters as liquid Si to filament contact angle, frequency of spurious Si grain nucleation at the filaments, thermal expansion match to silicon in the temperature regime below the Si plastic deformation temperature (650°C), sheet purity, and sheet electrical/photovoltaic performance. A number of filament materials were shown to be suitable for edge-supported pulling of silicon sheet crystals.

The materials studied were graphite and quartz solid filaments, SiC-coated graphite, SiC fibers, graphite yarn, Graphoil® graphite paper, carbon felt, vitreous carbon, mullite, sapphire, and thin-wall quartz capillaries. The dense graphite filaments were 1.5 mm diameter machined rods. By passing the rods through a 1550-1600°C silicon melt at a rate of 2 mm/min, SiC-coated graphite filaments were produced. Another type of SiC filament was investigated. This was an SiC solid fiber (an experimental product of the Dow Corning Corporation). Those used in this study were about 0.06 mm in diameter. Because of their small diameter, these filaments flexed excessively when contacting the liquid silicon. However, they were not available in long enough lengths to pull through the melt under tension. The graphite yarn was a multistrand product with an effective diameter of 0.5–0.6 mm when twisted and pulled through the melt under tension. Graphoil®, a registered product of the Union Carbide Corporation, is a thin, paper-like form of graphite. Filaments with a rectangular cross section of about 0.2 × 5 mm were cut from the material. The carbon felt filaments, 0.7 × 4 mm in cross section, were cut from a 0.7 mm thick carbon felt sheet. The vitreous carbon and mullite filaments were prepared by making longitudinal cuts with a diamond saw through crucibles of the material. The vitreous carbon filaments were 1.1 × 2.4 mm in cross sec-

tion, and the mullite filaments were 1.1 × 1.3 mm. The sapphire filaments were 0.3 × 3.4 mm in cross section and were cut from 0.3 mm thick sapphire wafers. The quartz filaments and capillaries were produced by drawing techniques. Various diameters and wall thicknesses were tested.

The very pliable graphite multistrand yarn was used in the semicontinuous configuration of fig. 1. It was pulled upward, under tension, through the crucible bottom. The other materials possessed enough rigidity so that tests could be performed on approximately 40 mm long samples by immersing them in a deep melt until the seeds contacted the liquid and then pulling them upward to grow the sheets. We have used graphite and quartz filaments in both short and semicontinuous configurations.

Silicon seeds with a (110) surface were used to bridge the filaments and initiate growth. In most cases, it was possible to initiate single or nearly single crystal growth. One of the objectives of this investigation was to study quantitatively the spurious grain nucleation at the sheet edges for the various filament materials. All filaments with a rectangular cross section were mounted with the wide surface parallel to the sheet. After the liquid meniscus was formed between the filaments and seed, the growing sheet was pulled upward at relatively slow speeds (5–15 mm/min) to achieve a long contact time between filaments and the melt and hence to enhance the probability of incurring detrimental effects of the filaments upon the sheet properties. The speed was adjusted as required to maintain uniform thickness at a given hot-zone temperature. No investigation was made of growth rate dependence upon filament material. Fresh semiconductor-grade silicon melts were used each time filaments containing different elements were investigated. All melts were doped with boron to approximately 2 Ωcm, p-type.

After growth, several parameters were studied. Cross sections through the filament and sheet were cut and lapped to measure apparent silicon/filament contact angles. Longitudinal sections were similarly prepared and etched to investigate spurious grain nucleation at the sheet/filament boundary. Large (up to 2 cm × 2 cm) sheet sections were lapped and etched to observe grain structure in the sheets and to provide substrates for solar cell fabrication. Solar cell parameters were compared to those of coprocessed Czochralski-grown control cells. All cells were the diffused junction type with phosphorus-doped n-type layers and a multilayer antireflection coating.

Figure 7 shows longitudinal and cross sections of the filament/silicon contact regions for two representative filament materials, quartz capillaries

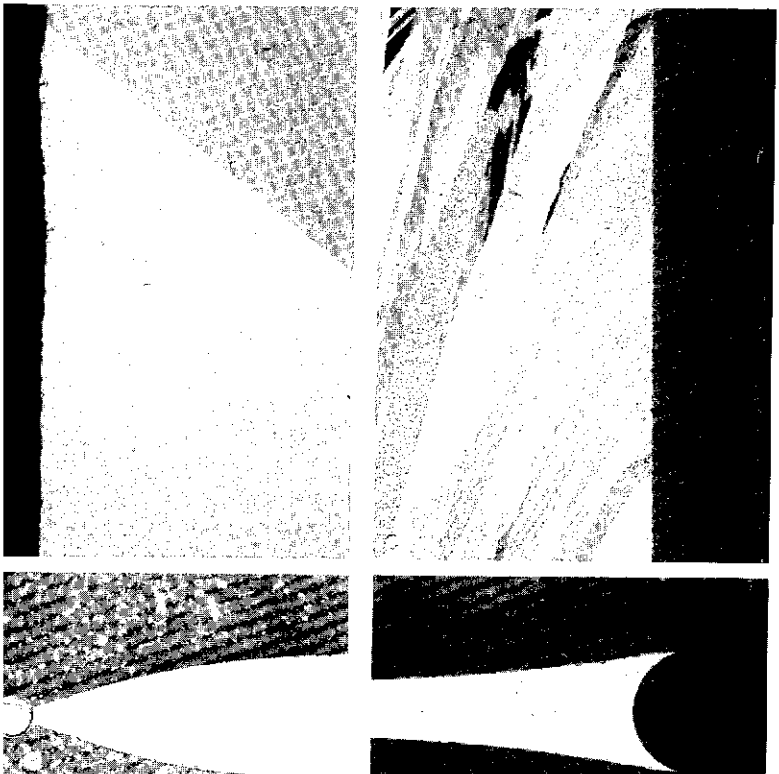

Longitudinal and cross sections near the filament for quartz capillary (a and b) and rod (c and d) filaments. In (a), the filament has separated from the sheet due to expansion mismatch. In (b), a portion of the capillary filled with Si and adhered to the sheet. The width of the photomicrographs is 5 mm.

in graphite rods. From such cross sections, the apparent contact between the filament and silicon was measured for the different nt materials. The etched longitudinal sections render a measure of mber of grains nucleated per unit length of the filament. The linear / was measured parallel to the filaments, 1 mm away from the sheet/ nt boundary. These quantities are given in table 2 for the various nt materials. Two natural groupings are seen. All carbon-containing

Table 2
Apparent co

Filament
Graphite
SiC-coated g
Graphite yarn
SiC fiber
Carbon felt
Graphitic pap
Vitreous carb
Mullite
Quartz
Sapphire

filaments h
large densi
large (>75
In general,
the contact
not be mea
tions at the
paper), con
thermal she
phire). In t

Thermal
of a filamen
mal expansi
for silicon b
ature. Some
to silicon. C
poorer ther
silicon sheet
of the sheet
able therma
extensively
stress could
sion coeffici
within the s

Table 2
Apparent contact angle between filament and silicon, and density of grain nucleation.

Filament	Contact angle (deg)	Nucleation density (grains/cm)
Graphite	12	30
SiC-coated graphite	11	80
Graphite yarn	<15	60
SiC fiber	<15	65
Carbon felt	<15	60
Graphite paper	<15	45
Vitreous carbon	<15	60
Mullite	77	6
Quartz	91	3
Sapphire	>75	7

filaments have small (<15°) contact angles with silicon and nucleate a large density of spurious grains (about 60/cm). All oxide filaments have large (>75°) contact angles and nucleate few spurious grains (about 5/cm). In general, the area of contact between filament and sheet is small when the contact angle is large. For some filaments, the contact angles could not be measured because of large curvature or irregular surface undulations at the point of contact (SiC fibers, vitreous carbon, and graphite paper), complete wetting of the filament (carbon felt, graphite yarn), or thermal shear-stress separation of the filament from the Si sheet (sapphire). In these cases a qualitative value of the angle is given.

Thermal expansion mismatch is a significant consideration in the choice of a filament material for edge-supported pulling. Figure 8 shows the thermal expansion coefficient for the rigid filament materials investigated and for silicon between room temperature and its plastic deformation temperature. Some graphites, vitreous carbon, and mullite are closely matched to silicon. Other graphite grades, SiC, sapphire, and quartz have a much poorer thermal expansion match. These materials lead to fracturing of the silicon sheet (and in some cases, the filament) at some point in the cooling of the sheet to room temperature. Some SiC fibers, however, have a tolerable thermal expansion coefficient match to silicon and have been used extensively for ESP growth (Cook and Sachs, 1982). The thermal shear stress could be estimated for graphite rod filaments with a thermal expansion coefficient of 7.7×10^{-6}/K, since in this case, the fracturing was within the silicon sheet. One end of the ribbon was intact, and the split

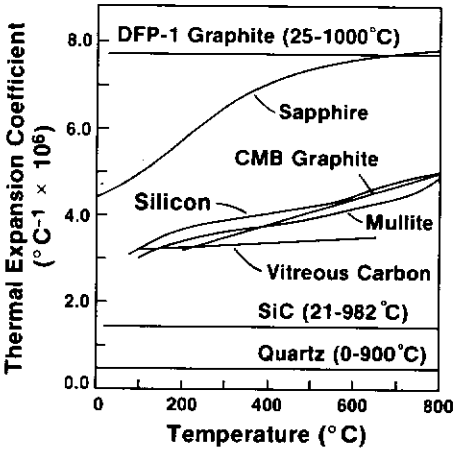

Fig. 8. Thermal expansion coefficients of silicon and some filament materials. For DFP-1 graphite, SiC, and quartz, the horizontal lines represent average values over the indicated temperature range.

width s increased with L, the distance from the intact end. An estimate of the stress σ is then obtained from $\sigma = WYs/4L^2$, where W is sheet width and Y is Young's modulus [1.9×10^{12} dyn/cm^2 for (111) silicon]. In this case W was 3.4 cm and s was 6 cm at $L = 24$ cm, giving a value of 1.7×10^{10} dyn/cm^2 for the stress σ.

The thermal expansion mismatch problem is particularly severe for filament materials that the silicon wets well. However, the mismatch can be used to advantage for poorly wetting filaments, especially if the filament can be made weak relative to the silicon sheet. For example, with quartz filaments, it is observed that 0.5–1.0 mm diameter capillaries with a 0.02–0.05 mm wall thickness will allow intentional thermal stress separation at the sheet/filament boundary with negligible sheet damage (fig. 9). Smaller diameter capillaries deform excessively in the melt, while 1 mm or larger capillaries with a thicker wall, or which are solid, severely fracture the silicon sheet. Although only thermal shear stresses arising from thermal expansion mismatch between filament and silicon sheet have been considered here, other thermal stresses are present due to uneven cooling, especially for wide ribbons.

Impurity analyses were conducted on silicon sheets grown using graphite, graphite yarn, and mullite filaments. Fourier transform infrared

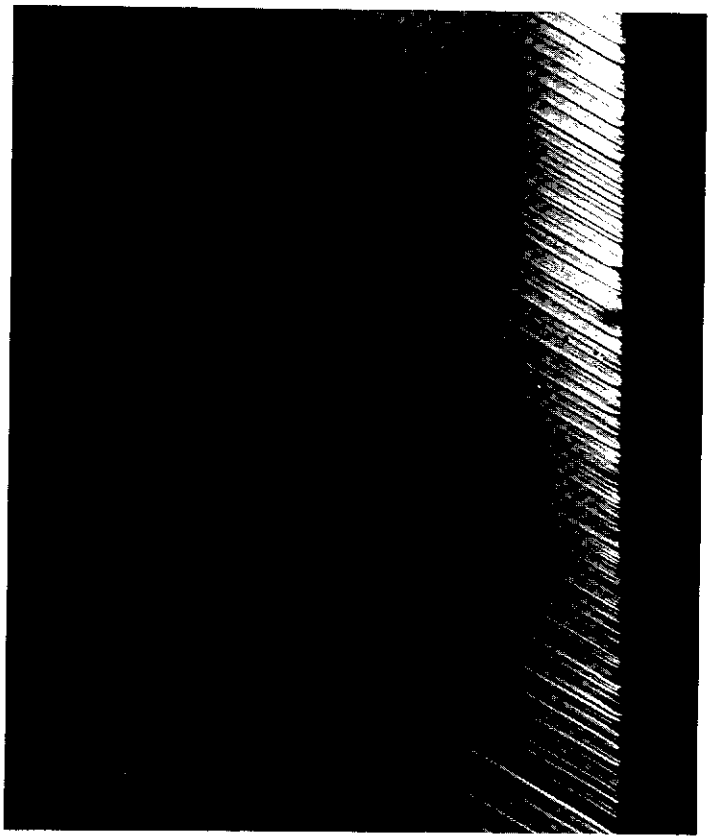

Fig. 9. Photomicrograph showing a silicon sheet cleanly separated by thermal stress from a 0.5 mm diameter quartz capillary filament with 0.02 mm wall thickness.

spectroscopy was used to measure oxygen and carbon levels, and a mass spectroscopy search for other impurities was conducted (see table 3). The carbon and oxygen levels observed are similar to those in Czochralski-grown silicon crystals. The measurement accuracy is estimated to be ± 1 ppma. The mass spectroscopy analyses were performed with a general-purpose analytical machine (not dedicated to silicon analysis) and are probably only accurate to within a factor of 3 (dopant impurity levels do not correlate well with resistivity measurements, for example).

Planar sheets suitable for solar cell fabrication were obtained with all the filament materials except SiC fibers and graphite paper. In those two

Table 3
Impurity analysis of silicon sheets grown using graphite, graphite yarn, quartz, and mullite filaments.

	Concentration (ppma)			
Impurity	Graphite	Graphite yarn	Quartz	Mullite
B	0.1	0.05	0.03	0.03
C[a]	15	15	<1.4	<1.9
O[a]	4	8	8	7
Mg	0.03	0.05	0.1	0.1
Al	0.05	0.1	0.2	0.3
P	0.2	0.3	0.1	0.2
Cl	0.1	0.03	0.5	0.1
Ca	0.1	0.1	–	0.2
Cr	0.03	0.02	0.2[b]	0.05
Mn	–	–	0.03[b]	–
Fe	0.1	0.1	1.0[b]	0.1
Cu	0.02	0.03	0.5[b]	0.02
As	–	0.01	–	–

[a] Measured by FTIR spectroscopy; others by mass spectroscopy.
[b] Inhomogeneous.

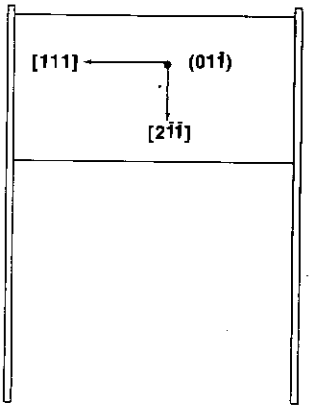

Fig. 10. Seed orientation for twin-plane blocking of spurious grains nucleated at filaments.

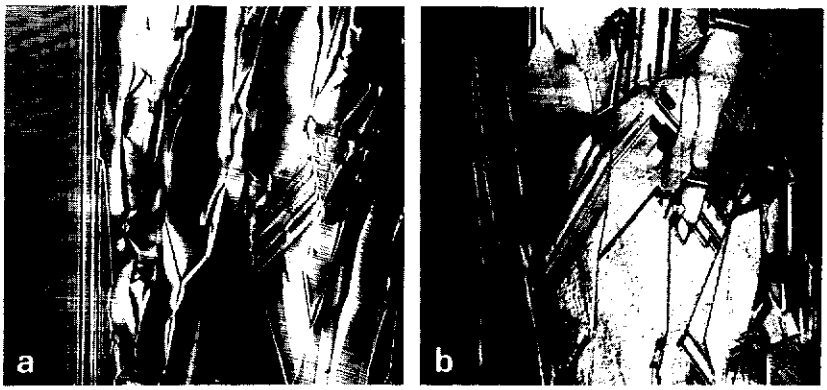

Fig. 11. (a) Optical photomicrograph (2 mm field width) of seeded sheet surface near filament showing twin-plane blocking of spurious grains. (b) Optical photomicrograph (2 mm field width) of unseeded sheet surface near filament.

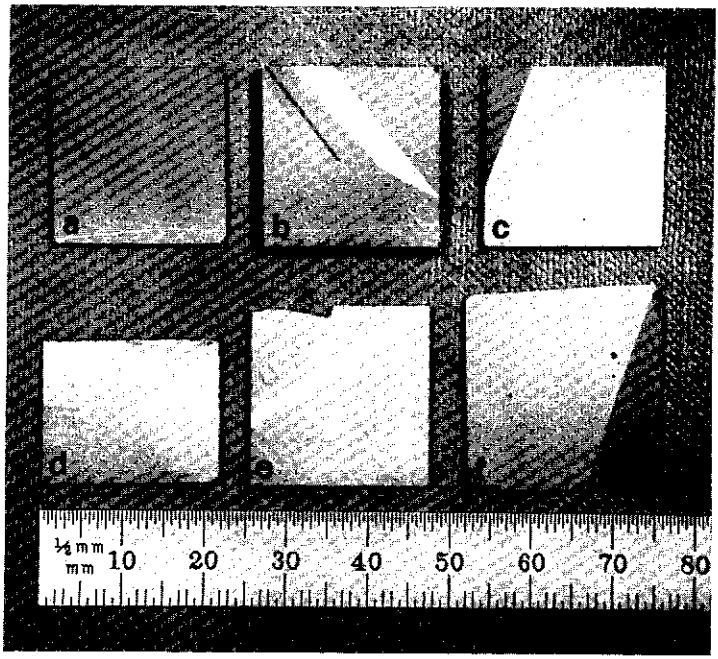

Fig. 12. Photograph of NaOH-etched, 2 cm wide wafers removed from midregion of sheets grown with different filament materials: (a) mullite, (b) sapphire, (c) quartz, (d) carbon felt, (e) SiC-coated graphite, and (f) vitreous carbon.

cases, flexing of the filaments warped the sheets grown in the dipping mode. As previously reported, grain widths on the order of 1 cm are attainable in the central regions of seeded sheets grown from graphite filaments (Ciszek and Hurd, 1980). Similar results were found in this study for the other carbon-containing filaments and oxide filaments. The use of (110) surface seeds with (111) parallel to the filaments and perpendicular to the sheet (see fig. 10) frequently results in twin-plane blocking of spurious grains nucleated at the filaments. Hence, a relatively large-grain structure prevails in the central portion of the sheet for the relatively short ribbons studied here. Figure 11 illustrates this twin plane blocking mechanism. Figure 12 shows the grain structure in 2 cm wide rectangular wafers cut from the midregion of sheets grown with the various filament materials. The wafers were lapped and etched in an NaOH solution to show the grain structure. The predominant boundaries are twin planes.

Even unseeded sheets have relatively large grains in the central region.

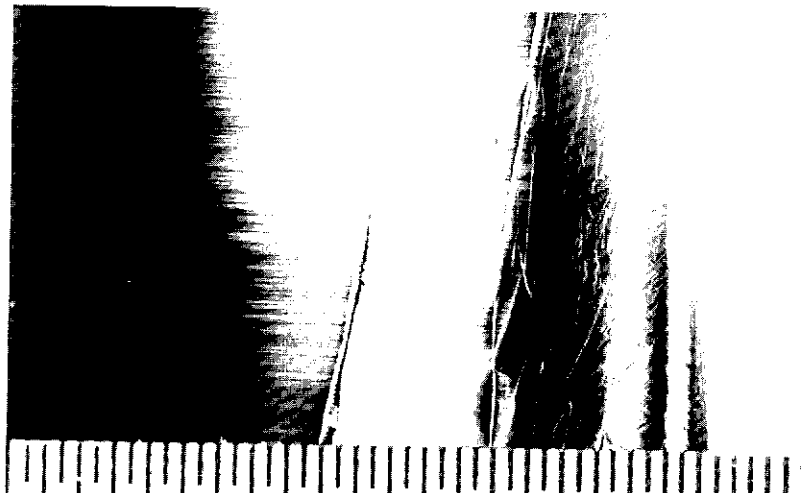

Fig. 13. Photograph of one-half the ribbon width for an unseeded 40 mm wide Si sheet. The distribution of grain size from the filament (right) to the sheet axis (left) can be seen.

Figure 13 is a photograph showing the distribution of grain sizes from the filament (right) to the axis (left) of a 40 mm wide unseeded sheet grown with graphite filaments. A fine-grained region with less than 1 mm grain size is observed within 4–5 mm of the ribbon edge, while larger grains are present in the remainder of the sheet. We have not yet investigated the solar cell performance of the fine-grained region.

5. Photovoltaic performance of ESP sheets

Diffused-junction solar cells were fabricated on the wafers of fig. 12, as well as on wafers from sheets grown with graphite filaments and on single crystal Czochralski-grown control wafers. Photovoltaic performance of the various wafers is shown in table 4. The cell parameters for sheets grown with the different filament materials are expressed as fractions of the values for the coprocessed Czochralski-grown control cell. For most of the wafers, the control cell parameters were short-circuit current density, J_{sc} = 31 mA/cm^2; open-circuit voltage, V_{oc} = 580 mV; current vs. voltage curve fill factor, FF = 79.4%; and cell efficiency, η = 14.1%. The exception was the sheet grown with graphite yarn filaments, where the control

Table 4
Solar cell performance of sheets grown with different filaments.

	Solar cell AM1 parameters as a fraction of control parameters					
Filament material	J_{sc}	V_{oc}	FF	η	η	Resistivity (Ωcm)
	(31.0)	(580)	(79.4)	(14.1)	(%)	
CZ control	1.00	1.00	1.00	1.00	14.1	2.7
Graphite	0.93	0.98	0.94	0.85	12.1	–
Graphite yarn	0.92	0.98	0.96	0.87[a]	10.8	–
Vitreous C	0.86	0.97	0.99	0.83	11.7	1.93
Carbon felt	0.97	0.98	0.97	0.92	13.0	–
SiC/graphite	1.0	0.99	0.94	0.93	13.1	3.30
Quartz	0.96	0.98	0.99	0.93	13.1	2.88
Mullite	0.94	0.98	0.98	0.90	12.7	1.96
Sapphire	0.91	0.97	0.97	0.85	12.0	4.47

[a] Control cell efficiency was 12.4% for this ribbon.

cell parameters were J_{sc} = 29 mA/cm^2, V_{oc} = 581 mV, FF = 74%, and η = 12.4%. The cell parameters were measured under the solar simulator of the Solar Energy Research Institute at AM1 conditions. Table 4 also lists the AM1 efficiency of each cell and, where available, its substrate resistivity.

All filament materials produced sheets capable of yielding cells that were at least 83% as efficient as the controls. Carbon-felt, SiC-coated graphite, quartz, and mullite yielded cell efficiencies that were 90%–93% of the control cell efficiencies. These four cells were 12.7%–13.1% efficient at AM1. For most of the filament materials, the degradation was primarily in J_{sc}. SiC-coated graphite gave excellent J_{sc}, with primary losses in fill factor. The graphite filaments showed losses in both J_{sc} and fill factor. In the case of carbon felt, J_{sc}, V_{oc}, and fill factor were all at least 97% as high as the values obtained on the control cell.

Solar cells fabricated from unseeded ESP sheets grown on graphite filaments yielded AM1 conversion efficiencies ranging from 7.4% to 12.6% with 10.0% as an average. Similar seeded sheets produced cells ranging

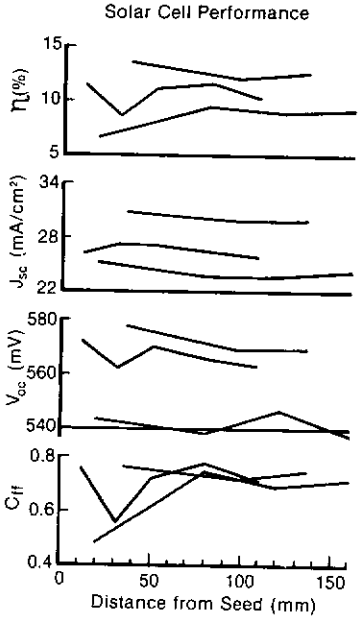

Fig. 14. AM1 solar cell characteristics as a function of length for three ESP sheets.

from 10.1% to 13.8% in efficiency, with a 13.0% average. The cells were 2 cm × 2 cm in size, with n-type diffused junctions on 2–3 Ωcm p-type sheets. Multilayer antireflection coatings were used. Total area efficiencies are reported.

Figure 14 shows solar cell characteristics as a function of the ribbon length for three crystals grown using graphite rod filaments, which underwent standard industrial solar cell processing. Each line represents one sheet, all pieces of which were cut and processed with the same batch by the same manufacturer. The varying and anomalously low efficiency values are attributed to differences in processing and do not reflect accurately the optimum for this material. Material quality does not appear to degrade with length. The highest AM1 conversion efficiency obtained to date for ESP material in semicontinuous sheets is 13.4%. The highest efficiency obtained for ESP material (seeded) to date is 13.8% (Ciszek and Hurd, 1980). When compared to Czochralski cells processed at the same time under the same conditions, the highest ESP efficiency/CZ efficiency ratio is 0.93.

6. ESP growth from metallurgical-grade silicon

The selling price of silicon escalates rapidly as its purity, crystallinity, and form evolve from mined quartzite to a polished, dislocation-free, high-purity wafer (see fig. 15). Ribbon growth is, in itself, an attempt to reduce or limit some of the cost increases. If useful sheets could be grown directly from metallurgical-grade silicon or upgraded metallurgical-grade silicon, even greater savings could be realized.

Direct conversion of two types of metallurgical-grade silicon (Union Carbide and Dow Corning direct arc reactor or D.A.R.) into sheet form has been carried out using ESP (Ciszek et al., 1981). Because of relatively high impurity levels in metallurgical-grade silicon, constitutional supercooling can occur. An unstable solid/liquid interface accompanies this phenomenon, and erratic localized deviations from planarity as large as 0.4 mm are observed. Because ESP growth is characterized by a 7 mm high meniscus and very good thermal stability is provided by the edge filaments, this growth method is relatively insensitive to disruption by interface instability. Sheet growth methods which require a specific crystallographic orientation or which are characterized by a narrow melt meniscus are most affected by irregularities at the solid/liquid interface.

It is likely that any form of low-cost silicon will have higher impurity

levels than those in semiconductor grade silicon, and hence it is important to investigate crystal growth problems related to impurities.

Prior to growth, the metallurgical silicon was etched for 20 min in an acid mixture composed of 1 part HF (48%) : 2 parts CH_3COOH (glacial) : 3 parts HNO_3 (70%), rinsed thoroughly, and dried. A graphite 'seed' or bridge was used to initiate growth in an argon ambient. The graphite

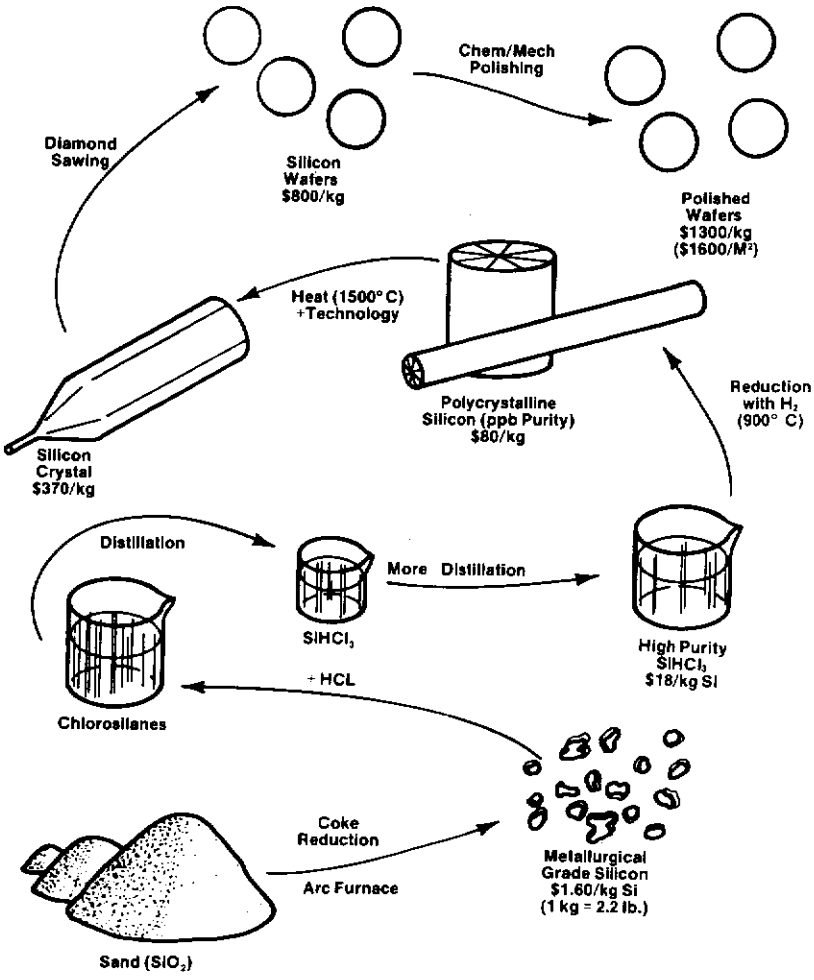

Fig. 15. Semiconductor silicon process sequence.

filament spacing was typically 4–5 cm. In some cases, a floating slag appeared on the liquid silicon surface after melting the metallurgical material. When this happened, a graphite skimmer was used to achieve partial removal.

Growth was conducted in both batch and continuous modes. In batch growth, up to eight sheets approximately 5 × 4 cm in size were solidified from a single melt by repeated dipping and withdrawal of filament assemblies. Growth speeds ranged from 10 to 18 mm/min. No evidence of constitutional supercooling-induced morphological surface undulations was seen. In the continuous growth mode, flexible filaments were passed through small openings in the crucible bottom as the solidifying sheet was pulled from the free melt surface. The pulling mechanism of our apparatus limits length to about 0.2 m, but growth can be reinitiated. Three long sheets were pulled from a shallow 75 g Union Carbide metallurgical melt, so that over 50% of the melt was solidified. Samples were removed at intervals along the sheets for impurity analysis to estimate impurity distributions.

A wide range of surface morphologies appears on sheets grown from metallurgical-grade silicon. There is not a consistent behavior from run to run, indicating that the impurity content of the metallurgical silicon is variable. With a given melt composition, reduced growth rates seem to decrease the magnitude of the protuberances if they are present. Growth has been conducted at speeds up to 30 mm/min without protuberances occurring with both Union Carbide and Dow Corning materials.

Some representative morphologies and corresponding surface profiles for the continuous growth mode are shown in figs. 16 and 17. Figures 16a and 17a show smooth growth, free of constitutional supercooling, from D.A.R. silicon at a growth speed of 19 mm/min. In figs. 16b and 17b, Union Carbide silicon and a 10 mm/min growth rate were used. The surface is slightly rougher, and in particular some grain boundary ridges and numerous surface particles are present. The particles tend to nucleate solid/liquid interface instabilities in the presence of constitutional supercooling. The effect can be seen on a very small scale in fig. 16b and will be discussed in more detail later. In figs. 16c and 17c, substantial cellular growth and some branching dendrites are seen. The same Union Carbide melt yielded the structures in figs. 16b, 16c, and 16d, but at progressive stages of solidification (i.e., about 0.08, 0.25, and 0.43 fraction solidified, g). The growth speed for fig. 16c was 14 mm/min. In figs. 16d and 17d, profuse dendrite structures are present and a cellular substructure radiates

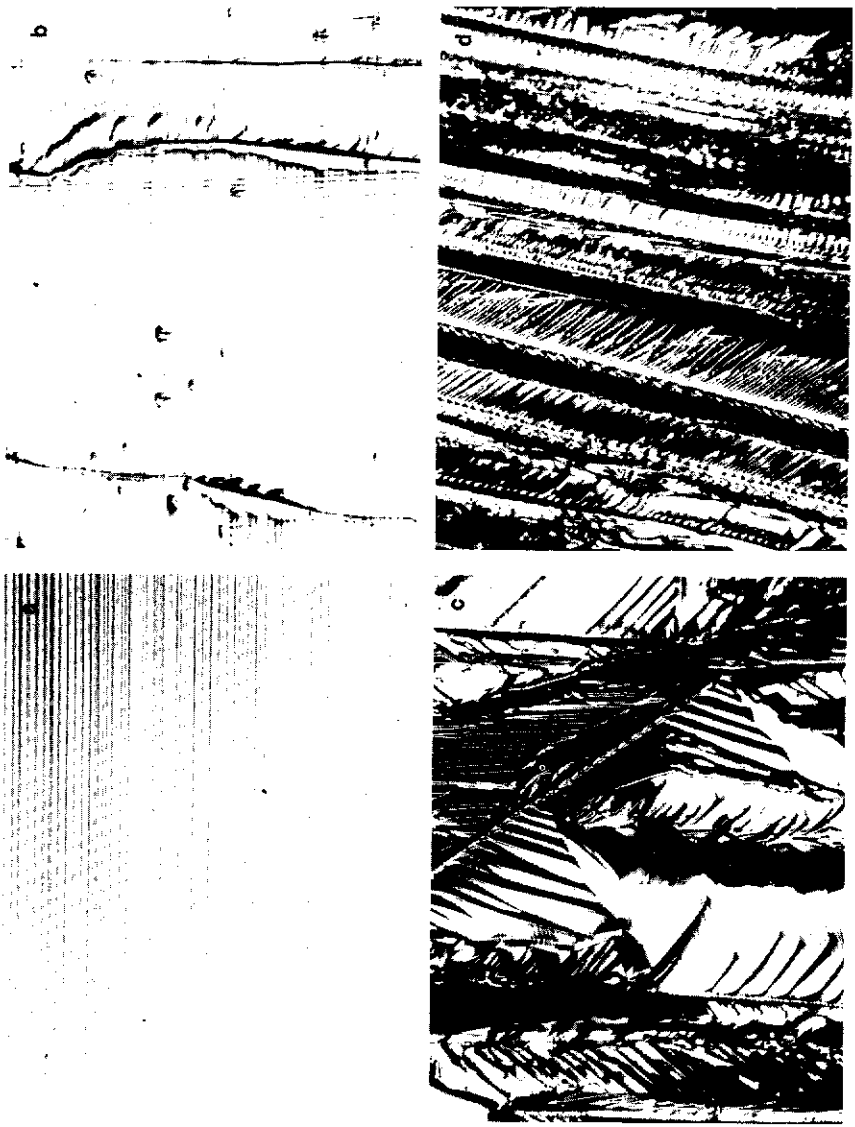

Fig. 16. A range of surface morphologies exhibited in ESP metallurgical silicon sheets.

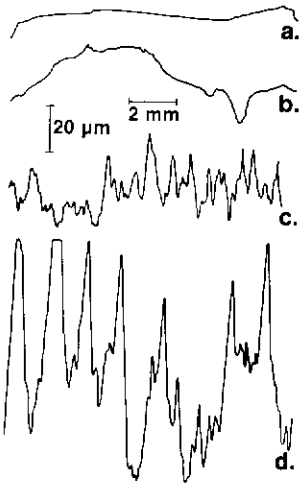

Fig. 17. Surface profiles corresponding to the morphologies of fig. 16.

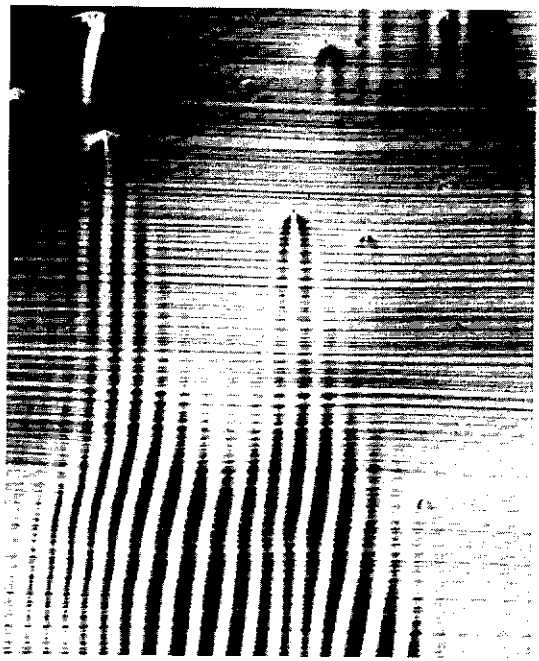

Fig. 18. Onset of cellular structure initiated by surface particles (0.9 mm picture width).

from the dendrites. Here, the growth speed was 11 mm/min. The peaks and valleys associated with the dendrites are the main contributors to the surface roughness and are on the order of 80 μm.

Surface particles of the type seen in fig. 16 can initiate cellular growth, as detailed in fig. 18. With constitutional supercooling, a positive gradient of supercooling exists in the liquid ahead of the solid/liquid interface. As pointed out by Rutter and Chalmers (1953), the interface is unstable in such a gradient since the growth rate is increased for any localized segment of the interface that advances ahead of the general interface. As the protuberance advances into the higher-temperature, lower-solute-content liquid ahead of the general interface, lateral rejection of solute retards growth at the base of the protuberance and enhances the probability of new protuberances being initiated around the original one. The result is a structure composed of close-packed, solute-poor cells separated by solute-rich cell boundaries. We feel that the role of the foreign particles is to provide a sudden advance of the interface as the particle is attached to it.

The question of the origin of the particles arises. The particle composition has been identified as SiC. Carbon filaments are used in the growth process, but particles have not been observed when high purity silicon material is used. We speculate that the particles originate in the metallurgical silicon, perhaps during the arc-furnace coke reduction of quartzite. Silicon carbide is slightly denser than liquid silicon, and it might be thought that the particles would sink to the crucible bottom as the metallurgical silicon is melted. However, a calculation using the Stokes formula indicates that the rate of descent is on the order of 2 mm/min for a spherical SiC particle 10 μm in diameter. It is thus feasible that convection currents could keep such particles in a quasi-suspended state. In addition to initiating cellular growth, the particles are known to be detrimental to high-quality epitaxial film growth on silicon substrates (Robinson, 1981).

The undulating surface morphology can also occur without being nucleated by particles. As shown in fig. 19, the surface consists of a series of linear plateaus separated by grooves approximately 2 μm deep. The plateaus are about 40–160 μm wide, and the valley half-width is about 10–20 μm.

There is no apparent dopant distribution correlation with the surface undulations (middle of fig. 19). The cellular structure extends partially through the sheet interior (bottom of fig. 19).

The grain size of sheets grown with a smooth surface or with a mildly undulating surface is on the order of 1–2 mm as shown in fig. 20. Sheets

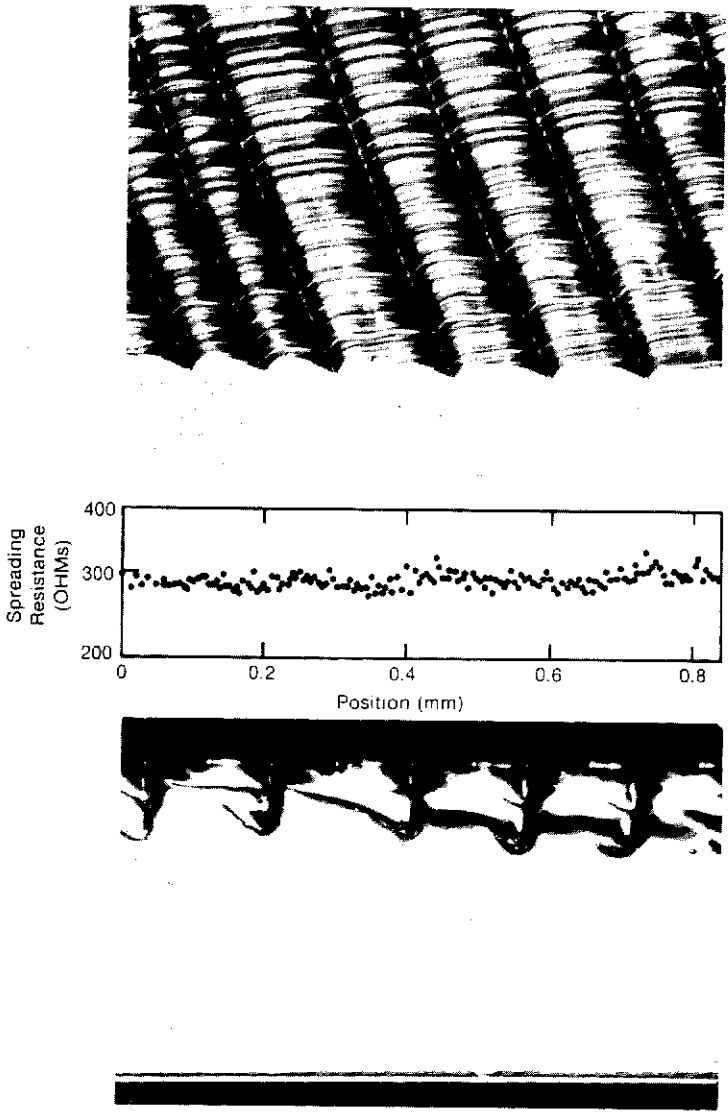

Fig. 19. Top: 5.7° beveled silicon sheet showing profile of surface undulations. Middle: Spreading resistance measurements at 5 μm intervals on beveled surface. Bottom: Solid/liquid interface pulled free of liquid. The cellular structure extends into the sheet about 1/4 of the sheet thickness.

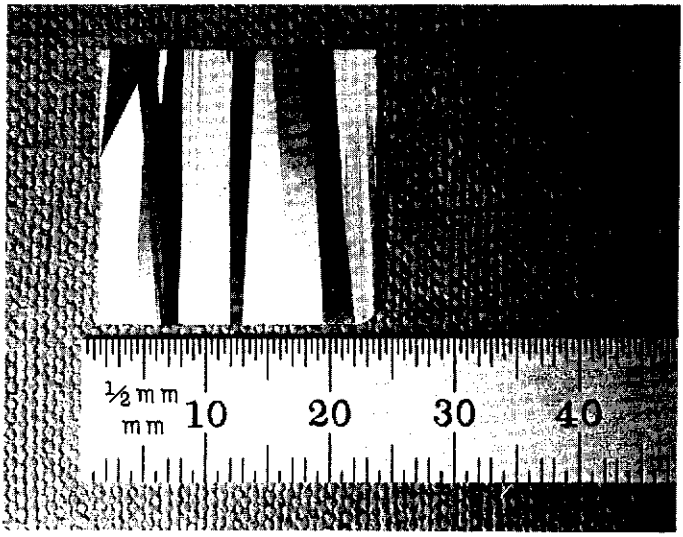

Fig. 20. NaOH etched surface of a sheet grown from D.A.R. silicon at 15 mm/min.

with dendrite and cellular surface features of the type in fig. 16 exhibit predominantly linear grains with fine spacing (about 0.01–0.3 mm). Particles of the type in figs. 16 and 18 are accompanied by dense dislocation networks that often extend along the sheet beyond the particle location.

Impurity segregation was found to be very effective when growth was conducted in the smooth, non-constitutionally supercooled mode. Table 5 gives spark-source mass spectroscopy results of impurity contents in the starting materials. Measurements were also made on ESP sheets grown from Union Carbide silicon in a continuous mode for both smooth growth and constitutionally supercooled growth. In each case, the measurements were made for the condition that the fraction of melt solidified was less than 0.25. Thus, when these values are divided by the impurity levels in the starting material, the ratio (called the 'removal ratio' in table 5) is approximately equal to the effective segregation coefficient for each impurity during ESP growth. The removal ratios for smooth ESP growth are generally larger than published values for normal-freezing segregation coefficients, but are small enough to allow considerable purification. In the cellular growth mode, the removal ratios are much larger and indicate that this mode of growth is not practical for solar cell substrates. As mentioned previously, there appears to be considerable variation in purity

Table 5
Impurity characteristics of metallurgical silicon and ESP sheet crystals.

Impurity	Concentration (ppmw)		Removal ratio ($g < 0.25$)		Amt. in G.B. / Amt. in grain (smooth ESP)
	MG silicon[a]	D.A.R. silicon[b]	Smooth ESP	Constitutionally supercooled ESP	
Al	>3300	100	<0.07	1	1.4
B	6.7	4	2	1	12.5
Ba	46	4	<0.002	0.05	–
C	80	–	0.05	1	1.8
Ca	410	100	<0.0002	0.08	2.2
Cr	74	2	0.01	1	5
Fe	>5000	200	<0.0001	<0.3	8.6
La	17	< 0.2	<0.006	0.4	–
Mg	73	5	0.002	0.2	3.3
Mn	1100	10	0.0004	0.5	3
Mo	4.8	< 2	0.02	0.4	–
Nd	< 11	< 1	0.01	0.3	–
Ni	83	4	0.01	1	> 1
P	16	3	0.2	0.8	–
S	8	2	0.08	0.3	–
Sr	13	< 2	<0.008	<0.008	–
Ti	500	50	<0.0002	1	6.7
V	460	2	<0.0002	0.2	> 1
Zr	42	< 2	<0.002	0.2	–

[a] Union Carbide.
[b] Dow Corning.

level of the starting materials and, hence, in the ability to grow smooth sheets. Impurity levels also vary considerably within ESP sheets, and it is difficult to assign an accuracy to the removal ratios reported in table 5. They are probably accurate to within a factor of 3.

One major variation within ESP sheets is that associated with grain boundaries. The last column of table 5 shows that for many impurities there is a higher concentration at boundaries than within adjacent grains. These data were obtained through quantitative secondary ion mass spectroscopy (SIMS) using a technique of in situ fracturing of the specimens under high vacuum (Kazmerski et al., 1980). The analysis is for smooth ESP sheets grown at 20 mm/min from Union Carbide metallurgical-grade silicon. The grain boundary/grain impurity ratio is particularly high for Ti,

Fe, Cr, and B. The metals are known to be detrimental to cell performance (Davis et al., 1978).

Both types of metallurgical-grade silicon produced p-type ESP sheets. For Union Carbide material, the average resistivity was 0.10 Ωcm, with a range of 0.05 to 0.23. For D.A.R. material, the average was 0.15 Ωcm, and the range was 0.10 to.0.23. The average diffusion length was 9 μm for both materials.

Table 6 gives solar cell characteristics for ESP sheets grown from the two types of metallurgical silicon. No doping was used during crystal growth, and the resistivities are lower than optimal. Union Carbide silicon achieved cell efficiencies about one-third as great as those of the high purity single crystal monitor cells, while the D.A.R. material yielded values up to one-half those of the control cells. Red response was relatively

Table 6
Solar cell data for metallurgical ESP silicon sheets.

No.	Si mat.	Cell by	Area (cm^2)	Res. (Ωcm)	Air mass	AR coat?	V_{oc} (V)	J_{sc} (mA/cm^2)	CFF (%)	EFF (%)
803	D	S	4.00	0.10	1	yes	0.54	19.3	0.52	5.2
8051	D	S	1.85	0.15	1	yes	0.56	18.9	0.73	7.0
8063	D	S	3.90	0.17	1	yes	0.55	17.2	0.67	6.3
2018	U	S	1.00	0.21	1	yes	0.48	20.0	0.33	3.3
2011	U	S	1.00	0.21	1	yes	0.40	24.0	0.32	3.1
CON.	CZ	S	4.00	1.9	1	yes	0.56	33.5	0.77	15.7
801	D	A	3.28	0.16	1	yes	0.56	15.6	0.72	6.3
8053	D	A	3.48	0.15	1	yes	0.56	15.4	0.73	6.3
2019	U	A	1.33	0.21	1	yes	0.53	15.2	0.60	4.8
406	U	A	3.96	0.06	1	yes	0.54	10.0	0.63	3.4
CON.	CZ	A	4.00		1	yes	0.59	28.4	0.73	12.2
601	D	R	0.86	EPI	1	yes	0.56	20.1	0.78	8.7
603	D	R	0.86	EPI	1	yes	0.57	20.4	0.81	9.4
804	D	R	0.86	EPI	1	yes	0.57	22.5	0.82	10.5
402A	U	R	0.73	EPI	1	yes	0.53	20.5	0.75	8.3
402B	U	R	0.77	EPI	1	yes	0.53	19.8	0.75	7.9
CON.	CZ	R	0.86	EPI	1	yes	0.58	22.6	0.80	10.6

D = Dow Corning S = Solarex U = Union Carbide A = ASEC R = RCA

poor for conventional cells made from both types of metallurgical grade silicon.

Epitaxial cells on D.A.R. substrates achieved efficiencies as high as 10.5%, and Union Carbide substrates yielded 8.3% epitaxial cells. All were small in area (≤ 0.86 cm^2). Fill factors were very high (up to 0.815).

7. Discussion

The relatively high solar cell efficiencies coupled with simplicity of sheet growth make ESP an attractive technique for terrestrial photovoltaics. Further work is required to explore the range of growth speeds, sheet thicknesses, and sheet widths achievable with this growth method. It is expected that maximum growth speeds for vertical pulling will be comparable to those of other vertical ribbon processes (Ciszek, 1976). There is no apparent theoretical limit to ribbon width. Increases in width and material throughput rate will be required to realize the full economic potential of ESP growth. One approach to enhanced growth speeds is to employ ESP in a near-horizontal configuration.

Numerous filament materials are viable for the edge-supported pulling sheet growth process. Graphite yarn, SiC, and quartz are attractive choices since they are available in very long lengths at relatively low cost. Carbon felt and graphite paper could be produced in moderately long lengths (10–100 m). Mullite, graphite, and vitreous carbon are noteworthy for their thermal expansion match to silicon. Quartz, on the other hand, can be geometrically designed to provide clean thermal shear-stress separation from the sheet. Sapphire, mullite, and quartz all nucleate very few spurious grains at the sheet/filament boundary. However, sapphire may not be an economical choice for a filament.

The ESP sheet growth method shows considerable promise as a technique for forming metallurgical-grade silicon sheets. High impurity levels in the starting material limit the efficiency of conventional cells made on such sheets to about 7%, and some form of material upgrading is necessary to achieve >10% AM1 AR-coated cell efficiencies. Epitaxial layer cells of the type described by Robinson et al. (1980) were capable of achieving 10% efficiencies on ESP metallurgical substrates. Growth anomalies induced by constitutional supercooling appeared to be more noticeable with Union Carbide silicon than with Dow Corning D.A.R. silicon, and the latter exhibited lower impurity levels and a lower density of SiC particles. Impurity segregation was effective in smooth ESP sheets,

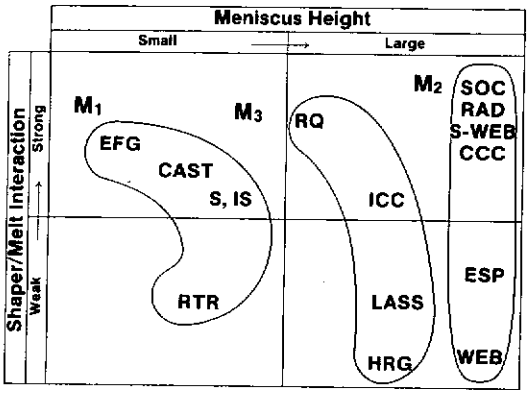

Fig. 21. Placement of the 15 sheet growth methods from table 1 by meniscus height and shaper/melt interaction.

but not in constitutionally supercooled sheets. A tendency for higher impurity levels at grain boundaries than within grains was seen.

As mentioned earlier, ESP is one of about 15 approaches to the growth of silicon sheets. It is in the category of 'high-meniscus' growth methods. In addition to meniscus geometry, the degree of shaper/melt interaction is a major factor in determining the PV performance of silicon sheets, since it can influence both grain size and purity levels. Figure 21 groups the various growth methods by both meniscus geometry and shaper/melt interaction. The three groups from left to right are associated with the M_1, M_3, and M_2 type meniscus. Within each group, the degree of shaper/melt interaction increases from bottom to top. Within the high meniscus (M_2) group, WEB has the least shaper/melt interaction, followed by ESP. The thermal control and ease of growing large widths are more favorable with ESP. The crystal perfection is better with WEB. The 'ideal' sheet growth method should possess good crystal perfection; flat, smooth surfaces; high purity; easy control; and high throughput. None of the existing techniques possesses all of these characteristics, but ESP shows encouraging progress as a compromise approach to achieving these attributes.

References

Belouet, C., J. Hervo, R. Martres, Ngo Tich Phuoc and M. Pertus, 1978, Proc. 13th IEEE Photovoltaics Specialists Conf., Washington, DC, 1978 (IEEE, New York) p. 131.

Boatman, J., and P. Goundry, 1967, Electrochem. Technol. **5**, 98.

Ciszek, T.F., 1972, Mat. Res. Bull. **7**, 731.

Ciszek, T.F., 1976, J. Appl. Phys. **47**, 440.

Ciszek, T.F., 1984, J. Crystal Growth, **66**, 655.

Ciszek, T.F., and J.L. Hurd, 1980, in: Proc. Symp. on Electronic and Optical Properties of Polycrystalline or Impure Semiconductors and Novel Silicon Growth Methods, St. Louis, 1980, eds. K.V. Ravi and B. O'Mara (The Electrochemical Society, Pennington, NJ) Vol. 80-5, p. 213.

Ciszek, T.F., and J.L. Hurd, 1981, US Patent Application Serial Number 238 234.

Ciszek, T.F., M. Schietzelt, L.L. Kazmerski, J.L. Hurd and B. Fernelius, 1981, Proc. 15th IEEE Photovoltaic Specialists Conf., Kissimmee, FL, 1981 (IEEE, New York) p. 581.

Ciszek, T.F., J.L. Hurd and M. Schietzelt, 1982, J. Electrochem. Soc. **129**, 2838.

Cook, E.J., and E.M. Sachs, 1982, Investigation of Edge-Supported Pulling of Silicon Ribbon, Final Report, SERI Contract No. XW-1-1069-1, 1983 (Solar Energy Research Institute, Golden).

Davis, J.R., A. Rohatgi, P. Rai-Choudhury, P. Blais, R.H. Hopkins and J.R. McCormick, 1978, Proc. 13th IEEE Photovoltaic Specialists Conf., Washington, DC, 1978 (IEEE, New York) p. 490.

Dermatis, S.N., and J.W. Faust, Jr., 1963, IEEE Trans. Commun. Electronics **82**, 94.

Dietl, J., D. Helmreich and E. Sirtl, 1981, 'Solar' Silicon, in: Crystals–Growth, Properties, and Applications, Vol. 5, ed. J. Grabmaier (Springer-Verlag, Berlin) pp. 43–108.

Hurd, J.L., and T.F. Ciszek, 1982, J. Crystal Growth **59**, 499.

Kazmerski, L.L., P.J. Ireland and T.F. Ciszek, 1980, Appl. Phys. Letters **36**, 323.

Labelle, H.E., A.I. Mlavsky and B. Chalmers, 1971, Mat. Res. Bull **6**, 571, 581, and 681.

Maeda, Y., and T. Yokoyama, 1982, Proc. 16th IEEE Photovoltaic Specialists Conf., San Diego, 1982 (IEEE, New York) p. 133.

Robinson, P.H., 1981, private communication.

Robinson, P.H., R.V. D'Aiello and D. Richman, 1980, Proc. 14th IEEE Photovoltaic Specialists Conf., 1980 (IEEE, New York) p. 54.

Rutter, J.W., and B. Chalmers, 1953, Can. J. Phys. **31**, 15.

Tsuya, N., K.I. Arai, T. Takeuchi, K. Ohmor, T. Ojima and A. Kuroiwa, 1980, J. Electronic Matls. **9**, 111.

White, D.A., and J.A. Tallmadge, 1965, J. Fluid Mech. **23**, 325.

Zook, J.D., B.G. Koepke and B.L. Grang, 1980, J. Crystal Growth **50**, 260.